Open access • Journal Article • DOI:10.1107/S205252061800834X

(Al,Mg)3La: a new phase in the Mg–Al–La system — Source link

Charlotte Wong, Mark J. Styles, Su-Ming Zhu, Dong Qiu ...+5 more authors

Institutions: RMIT University, Commonwealth Scientific and Industrial Research Organisation, University of Queensland, Monash University

Published on: 01 Aug 2018 - Acta Crystallographica Section B Structural Crystallography and Crystal Chemistry (International Union of Crystallography (IUCr))

Topics: Powder diffraction, Orthorhombic crystal system, Scanning transmission electron microscopy and Crystal structure

STRUCTURAL SCIENCE CRYSTAL ENGINEERING MATERIALS

ISSN 2052-5206

$(Al,Mg)_3La$: a new phase in the Mg–Al–La system

Charlotte Wong,[a] Mark J. Styles,[b]* Suming Zhu,[a] Dong Qiu,[a] Stuart D. McDonald,[c] Yuman Zhu,[d] Mark A. Gibson,[a,b,d] Trevor B. Abbott[e] and Mark A. Easton[a]

[a]School of Engineering, RMIT University, Carlton, Victoria 3053, Australia, [b]CSIRO Manufacturing, CSIRO, Clayton, Victoria 3168, Australia, [c]School of Mechanical and Mining Engineering, University of Queensland, Brisbane, Queensland 4072, Australia, [d]Department of Materials Science and Engineering, Monash University, Victoria, 3800, Australia, and [e]Magontec Ltd, Sydney, New South Wales 2000, Australia. *Correspondence e-mail: mark.styles@csiro.au

Received 7 February 2018
Accepted 6 June 2018

Edited by R. Černý, University of Geneva, Switzerland

Keywords: $(Al,Mg)_3La$ phase; synchrotron powder diffraction; Rietveld refinement; simulated annealing; high-angle annular dark-field scanning transmission electron microscopy (HAADF-STEM) imaging.

Supporting information: this article has supporting information at journals.iucr.org/b

During an investigation of the Mg-rich end of the Mg–Al–La system, a new ternary phase with the composition of $(Al,Mg)_3La$ was identified. The crystal structure of this phase was determined by conventional X-ray powder diffraction and transmission electron microscopy analysis and refined using high-resolution X-ray powder diffraction. The $(Al,Mg)_3La$ phase is found to have an orthorhombic structure with a space group of $C222_1$ and lattice parameters of a = 4.3365 (1) Å, b = 18.8674 (4) Å and c = 4.4242 (1) Å, which is distinctly different from the binary Al_3La phase ($P6_3/mmc$). The resolved structure of the $(Al,Mg)_3La$ phase is further verified by high-angle annular dark-field scanning transmission electron microscopy.

1. Introduction

The high specific strength of magnesium alloys makes them attractive for use in transport applications where weight savings are important. However, the most common magnesium alloys such as AZ91 (Mg–9Al–1Zn) and AM60 (Mg–6Al–0.3Mn) tend to suffer from poor creep resistance, limiting their use in high-temperature environments (Luo, 2004). Alloys based on the Mg–Al–RE systems are found to have not only improved high-temperature creep resistance, but also a good balance of room-temperature mechanical properties (Zhu *et al.*, 2015), which leads to them being used in transport applications. The effects of individual rare-earth elements such as La and Ce on microstructure evolution and phase formation in Mg–Al alloys are poorly understood at present. Recent investigations by the authors on the Mg-rich end of the Mg–Al–La system have revealed some significant shortcomings in the published phase diagrams. In particular, the microstructures observed are often inconsistent with those predicted by solidification models based on the current thermodynamic databases.

Binary Al–La, Al–Mg and La–Mg phase diagrams have been developed and evaluated in the past (Zhou & Napolitano, 2006; Guo & Du, 2004; Liang *et al.*, 1998; Saunders, 1990; Yin *et al.*, 2000; Cacciamani & Ferro, 2001; Ansara *et al.*, 1997). The ternary Mg–Al–La phase diagram was first published based on experimental data collected prior to 1988 (Rogl, 1988). A partial isothermal section at 400°C for La concentrations up to 33.3 at.% was developed by Zarechnyuk *et al.* (1981). Following this, Odinaev *et al.* (1988) prepared and investigated 115 alloys, annealing them at 400°C for 480 h to develop an understanding of the phase equilibria at this temperature. The system was further investigated and

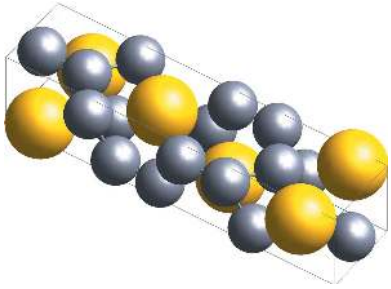

reviewed by Raghavan (2008). Recently, Hosseinifar & Malakhov (2010) studied two key alloys in the Mg–Al–La system and optimized the Mg–Al–La ternary phase diagrams. The Mg–Al–La thermodynamic database was also systematically evaluated and optimized by Jin *et al.* (2013). Table 1 summarizes the equilibrium solid phases currently reported in the Mg–Al–La system. It is worth mentioning that the individual RE elements, such as La and Ce, are often found to substitute within the Al–RE and Mg–RE intermetallic phases (Rzychoń *et al.*, 2013; Kleber *et al.*, 1970). For example, it is known that $Al_{11}La_3$ and $Al_{11}Ce_3$ are isostructural.

The research to date has tended to focus on commercial 'AE' magnesium alloys (A = Al, E = rare earth). Previous studies (Bai *et al.*, 2012; Zhu *et al.*, 2016) on AE alloys with lanthanum as the rare-earth element indicated that the main intermetallic phase is $Al_{11}La_3$ followed by Al_2La. In order to understand the discrepancies between the predicted and observed microstructures in Mg–Al–La alloys, a more detailed phase identification was performed using X-ray diffraction (XRD) and transmission electron microscopy (TEM). During this study, it was found that the main intermetallic phase in these alloys did not match the structures of the Al–RE phases commonly reported in these alloys, which are expected to be $Al_{11}La_3$ (Gomes de Mesquita & Buschow, 1967), Al_3La (Havinga, 1975) and Al_2La (Rao *et al.*, 1982). Here, we present the results of the characterization of a previously unreported intermetallic phase found in an Mg–4.5Al–6.3La alloy. The implications for understanding the microstructural evolution in AE alloys during solidification will be discussed elsewhere.

Table 1
Existing solid phases identified in the Mg–Al–La system.

Phase name (chemistry of phase)	Space group	Lattice parameters (Å)		
		a	*b*	*c*
$Al_{12}Mg_{17}$[a,b]	$I\bar{4}3m$	10.544	-	-
$Al_{30}Mg_{23}$[c,a]	$R\bar{3}$	12.825	-	21.748
Al_3Mg_2[c]	$Fd\bar{3}m$	28.2435	-	-
α-Al	$Fm\bar{3}m$	4.050	-	-
α-Mg	$P6_3/mmc$	3.210	-	5.211
$La_{22}Al_{53}$ (Al_5La_2)[a,d]	$P6/mmm$	4.478	-	4.347
$Mg_{17}La_2$[a,e]	$P6_3/mmc$	10.360	-	10.240
$Al_{11}La_3$[f,a]	$Immm$	4.431	13.142	10.132
$AlLa_3$[g,a]	$P6_3/mmc$	7.192	-	5.528
AlLa[d,a]	$Cmcm$	9.531	7.734	5.809
Al_3La[a,h]	$P6_3/mmc$	6.667	-	4.616
MgLa[i,a]	$Pm\bar{3}m$	3.960	-	-
$Mg_{12}La$[j,a]	$I4/mmm$	10.330	-	5.960
Al_2La[k,a]	$Fd\bar{3}m$	8.149	-	-
Mg_3La[l,a]	$Fm\bar{3}m$	7.478	-	-
$Al_{40}Mg_{17}La_3$[m]	-	-	-	-

References: (*a*) Villars & Calvert (1991), (*b*) Schobinger-Papamantellos & Fischer (1970), (*c*) Samson & Gordon (1968), (*d*) Buschow (1965), (*e*) Evdokimenko & Kripyakevich (1963), (*f*) Gomes de Mesquita & Buschow (1967), (*g*) Garde *et al.* (1993), (*h*) Havinga (1975), (*i*) Pierre *et al.* (1985), (*j*) Wood & Cramer (1965), (*k*) Rao *et al.* (1982), (*l*) Rossi & Iandelli (1934), (*m*) Jin *et al.* (2013).

Table 2
Composition of the Mg–4.5Al–6.3La (wt%) samples measured using the inductively coupled plasma–atomic emission spectroscopy method.

Sample	Elemental composition (wt%)						
	Al	La	Ca	Fe	Na	Si	Mg
Mg–4.5Al–6.3La	4.48	6.26	0.18	0.02	0.14	0.02	Bal (88)

2. Experimental procedure

2.1. Material preparation

An alloy with composition Mg–4.5Al–6.3La (wt%) was prepared from 99.9% pure Mg and Al, and 99.5% pure La by melting in an electric resistance furnace using a boron-nitride-coated stainless steel crucible. An inert cover gas was used to protect the sample from oxidation during melting. The composition of the sample was measured using inductively coupled plasma–atomic emission spectroscopy and the results are given in Table 2.

2.2. X-ray powder diffraction

Conventional XRD data were collected from a polished cross-section of the as-cast ingot using a Bruker D8 diffractometer fitted with a Cu X-ray tube (λ = 1.54059 Å). Data were collected between 5 and 140° 2θ using standard Bragg–Brentano geometry (Klug & Alexander, 1975) and a small linear strip detector. The flat plate sample was spun at ∼2 Hz in order to improve the particle statistics as much as possible.

High-resolution XRD patterns were collected using the Powder Diffraction beamline (Wallwork *et al.*, 2007) at the Australian Synchrotron. For the synchrotron data collection, a small amount of powder was filed from the as-cast alloy and sieved to obtain particles less than 75 µm in size. This powder was encapsulated in a glass ampoule under argon and annealed at 350°C for 2 h to relieve the stresses induced by filing. The powdered samples were packed into glass capillaries and studied in Debye–Scherrer geometry (Klug & Alexander, 1975). A monochromatic X-ray beam with a nominal energy of 18 keV was used and data were collected over the angular range 2–82.5° 2θ using the Mythen curved position-sensitive detector (Bergamaschi *et al.*, 2010). The capillaries were continuously rotated about their axes at ∼1 Hz during the measurement. A precise determination of the X-ray wavelength (λ = 0.68861 Å) was derived from diffraction patterns collected from a sample of LaB_6 (NIST SRM 660b). The diffraction patterns, which were acquired in pairs with the detector offset by 0.5° 2θ, were merged using the program *CONVAS2* (Rowles, 2010) in order to eliminate the gaps between the modules of the Mythen detector. The resulting merged data were then analysed by the Rietveld method (Rietveld, 1969), as implemented in the software package *TOPAS* (version 5, Bruker, 2014).

2.3. Electron microscopy

For microstructural examination a thin sample was cut from the cast ingot, mounted in epoxy resin and ground to approximately 15 µm. After grinding, the samples were then polished using cloth with diamond suspension to approximately 0.04 µm particle size. The samples were ultrasonically

cleaned between each step of grinding and polishing. The as-cast microstructure of each prepared sample was analysed using a Hitachi TM3030 scanning electron microscope (SEM) operating at 15 kV with a backscattered electron detector.

For TEM examinations, discs of 3 mm diameter and 0.1 mm thickness were cut from the bulk sample and ground, followed by low-angle ion milling using a Gatan Precision Ion Polishing System (PIPS). The TEM foils were examined in a Tecnai G2 T20 microscope, equipped with a Bruker Quantax 200 energy-dispersive X-ray (EDX) system. High-angle annular dark-field scanning transmission electron microscopy (HAADF-STEM) was conducted in a double-corrected FEI Titan^3 80-300 FEGTEM microscope operated at 300 kV. A 15 mrad convergence semi-angle was used, corresponding to a STEM resolution of 0.12 nm. HAADF-STEM images were acquired with the camera length set to give a collection semi-angle of 57–200 mrad. For better interpretability, raw HAADF-STEM images were processed by masking diffraction spots in the fast Fourier transforms of the original images and then back-transforming using the Gatan *DigitalMicrograph* software package.

3. Results and discussion

A typical SEM image and the conventional XRD data collected from the bulk sample of the Mg–4.5Al–6.3La alloy are shown in Fig. 1. The SEM image (Fig. 1*a*) reveals that the microstructure consists of primary α-Mg dendrites surrounded by a eutectic of α-Mg and intermetallic phase. For the XRD data (Fig. 1*b*), the peaks corresponding to the α-Mg phase can be readily identified; however, the observed intensities are not well modelled by the corresponding crystal structure. This is due to the poor particle statistics resulting from the large α-Mg dendrites present in the as-cast microstructure (Fig. 1*a*). Besides the α-Mg phase, the remaining peaks in this data set could not be satisfactorily identified using the International Centre for Diffraction Data PDF-4+ database (ICDD, 2017) or matched with other phases reported in the literature for Mg–Al–RE systems (Table 1).

The remaining peaks in the conventional XRD data were assumed to be from the same unknown phase and were indexed using the LSI method implemented in *TOPAS*. Several orthorhombic space groups matched the observed peaks well; however, taking into account systematic absences, the most promising candidate was identified as $C222_1$ (space group number 20) with lattice parameters a = 4.34, b = 18.96 and c = 4.43 Å. Both the α-Mg and the unknown phase were fitted using the Pawley (1981) method and the result is shown in Fig. 1(*b*). All of the observed peaks were accounted for using this method, suggesting that the sample is indeed composed of two phases without additional impurity phases.

TEM data were collected from samples of the as-cast Mg–4.5Al–6.3La ingot in order to determine the composition of the intermetallic phase and corroborate the space group identified using the XRD data. The low-magnification bright-field image, given in Fig. 2(*a*) shows a large number of intermetallic particles embedded on the α-Mg grains. EDX spot analyses performed on these particles indicate that the composition of the intermetallic phase is close to $(Al,Mg)_3La$ (*e.g.* Fig. 2*b*). The analysed particles were carefully selected to minimize the contribution of the Mg matrix and it is thought that the presence of a small amount of Mg in this phase is genuine, although it is difficult to quantify the Mg fraction precisely (the effects of Mg concentration on the structure of Al_3La will be the subject of a future investigation). Selected area diffraction (SAED) data were collected from the intermetallic particles and the results are shown in Fig. 2(*c*). Indexing of the SAED patterns and measuring of titling angles between the common zone axes confirm that the intermetallic phase has an orthorhombic space group with lattice parameters a = 4.34, b = 18.87 and c = 4.42 Å, in excellent agreement with the XRD data. It should be noted that there are reflections at the positions of (00l), $l = 2n + 1$, as a result of double diffraction. For example, the (001) spot can be produced by double diffraction from (021) and (0$\bar{2}$0).

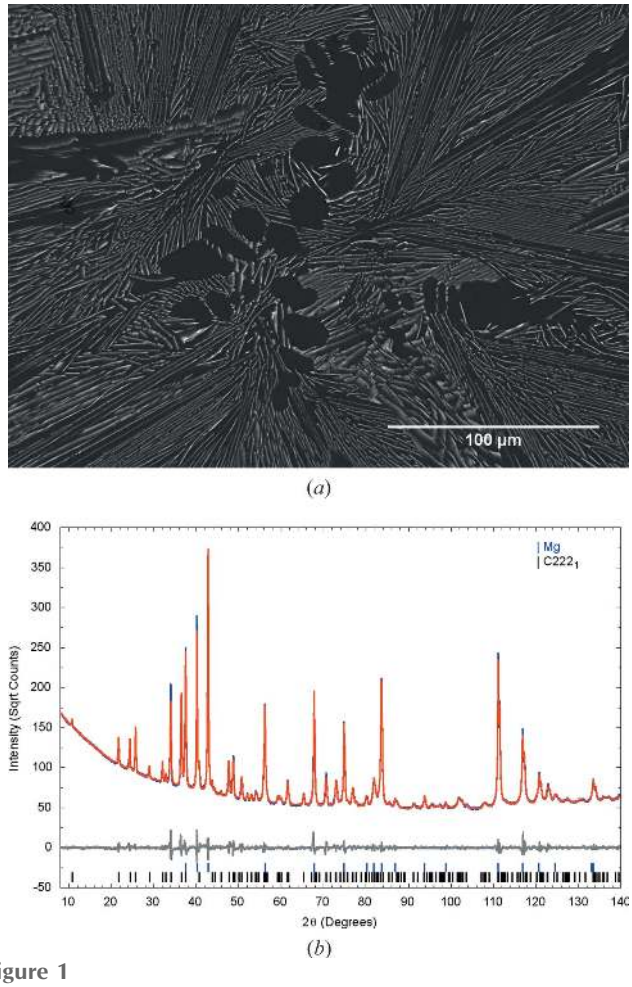

Figure 1
(*a*) SEM image from a bulk sample of the Mg–4.5Al–6.3La alloy. The microstructure consists of two phases, α-Mg (dark contrast) and a previously unreported La-containing intermetallic phase (bright contrast). (*b*) The corresponding XRD data have been fitted using the Pawley (1981) method. The intermetallic phase has an orthorhombic ($C222_1$) structure with lattice parameters a = 4.34, b = 18.96 and c = 4.43 Å. The observed, calculated and difference patterns are shown in blue, red and grey, respectively. The tick marks below the plot show the positions of the Bragg reflections for the two phases.

A preliminary structure determination was attempted using the conventional XRD data. Based on the TEM EDX results, a simplified composition of Al_3La was assumed due to the low X-ray scattering contrast between Al and Mg. The density of similar phases reported in the literature (*e.g.* Al_3La and $Al_{11}La_3$) range between 3.95 and 4.20 g cm^{-3}. Based on the unit cell volume and chemistry observed, it was determined that there should be four formula units per unit cell to give a density of ∼4.01 g cm^{-3}. Using this information, a structure determination was attempted using the simulated annealing method (Coelho, 2000). Four unique atomic sites were used, with one La atom and three Al atoms. In order to help identify special positions within the crystal structure, occupancy merge radii for the Al atoms of 1.0 Å and anti-bump radii of 3.0 and 3.3 Å for Al–La and Al–Al atom pairs, respectively, were used. Other refinable parameters, such as lattice parameters and background function for example, were fixed during the simulated annealing.

After several iterations it became apparent that the x and z coordinates of all four sites quickly converged on the special positions 0 and $\frac{1}{4}$, respectively (4*b* site), giving densities close to the target 4.01 g cm^{-3}. These coordinates were fixed in subsequent refinements, with only the y coordinate for each atom allowed to refine. This process resulted in a preliminary set of atomic coordinates of y = 0.10, 0.47, 0.33 and 0.75 for the La, Al1, Al2 and Al3 sites, respectively. However, due to the poor particle statistics evident in the α-Mg phase, the accuracy of this proposed structure was unclear.

To improve the reliability of the structure refinement, synchrotron data were collected from a powdered sample that had been annealed under argon to relieve stresses induced by the grinding process. The results from the synchrotron measurement are shown in Fig. 3. The particle statistics from the Mg phase were improved considerably, allowing the peak intensities to be accurately modelled using the Rietveld method. In addition to the $(Al,Mg)_3La$ phase of interest, a small amount (∼2 wt%) of magnesium oxide (MgO) was

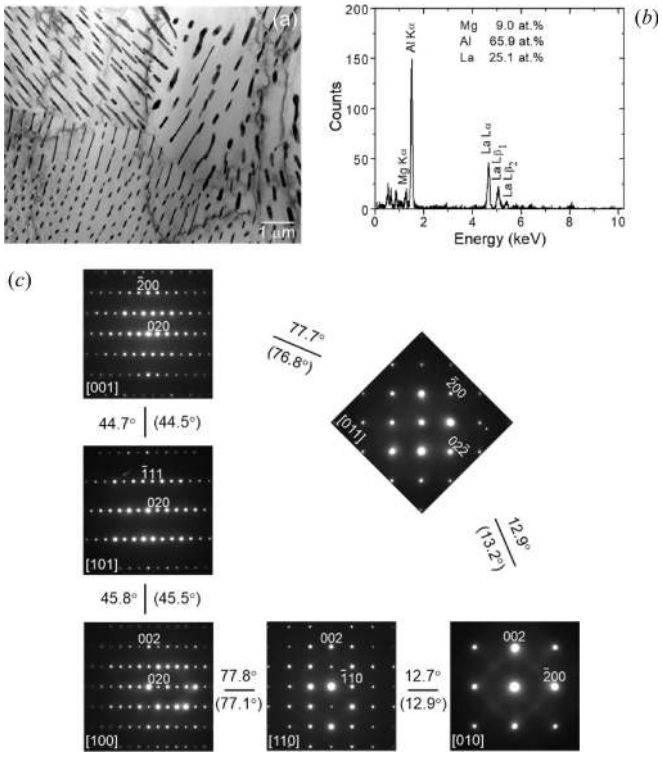

Figure 2
(*a*) TEM bright-field image, (*b*) EDX analysis and (*c*) a series of selected area diffraction patterns of the intermetallic phase in the Mg–4.5Al–6.3La alloy. The EDX spectrum suggested a composition close to $(Al,Mg)_3La$. The diffraction patterns could be well indexed according to the orthorhombic ($C222_1$) structure with lattice parameters a = 4.34 Å, b = 18.96 Å and c = 4.43 Å. The experimental tilting angles are close to those calculated (numbers in brackets).

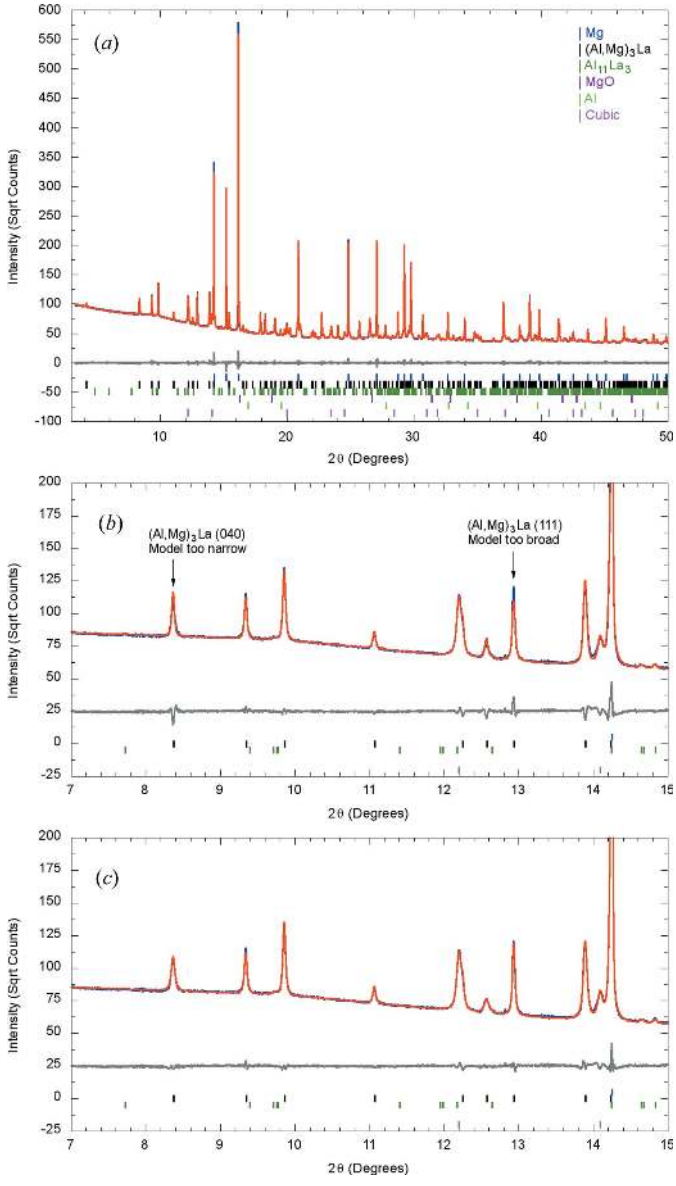

Figure 3
(*a*) Final fit to the synchrotron data for the powdered sample of Mg–4.5Al–6.3La. The observed, calculated and difference patterns are shown in blue, red and grey, respectively. (*b*) Enlargement of a preliminary refinement highlighting anisotropic broadening of the $(Al,Mg)_3La$ phase peaks (R_{wp} = 3.61%). (*c*) Improvement achieved in final fit using the Stephens (1999) method to model the anisotropic broadening (R_{wp} = 3.05%)

Table 3
Crystallographic parameters refined for the $(Al,Mg)_3La$ phase.

The uncertainties reported in brackets are 2× the estimated standard deviations (*i.e.* 2σ) calculated by *TOPAS*.

Formula	$(Al,Mg)_3La$
Density (g cm^{-3})	4.0342 (1)
Space group	$C222_1$
Lattice parameters *a*, *b*, *c* (Å)	4.3365 (1), 18.8674 (4), 4.4242 (1)
Volume (Å^3)	361.98 (1)

Atomic coordinates	*x*	*y*	*z*	Occupancy	B_{eq} (Å^2)
La	0	0.1043 (1)	0.25	1.0	0.70 (3)
Al1	0	0.4666 (4)	0.25	1.0	0.9 (2)
Al2	0	0.3342 (4)	0.25	1.0	0.9 (2)
Al3	0	0.7493 (4)	0.25	1.0	0.7 (2)

detected as a result of the annealing processes. The sample was also found to contain a very small fraction of the $Al_{11}La_3$ phase as well as a cubic phase with a structure similar to a mixed La–Ce oxide or La hydride ($Fm\bar{3}m$, a = 5.61 Å) (Korst & Warf, 1966; Sung Bae *et al.*, 2004). A trace amount of f.c.c. Al was detected, which is likely to be an impurity introduced during powder preparation.

The simulated annealing procedure described above was repeated for the synchrotron data, giving results in excellent agreement with the laboratory data. The final crystal structure parameters refined from the synchrotron data (using the Rietveld method) are given in Table 3 and a three-dimensional view of the crystal structure is given in Fig. 4. It should be noted that the high resolution of the synchrotron data also revealed a small amount of anisotropic broadening of the $(Al,Mg)_3La$ phase peaks, as highlighted in Fig. 3(*b*). In the final Rietveld analysis, the $(Al,Mg)_3La$ peak shapes were described using the Stephens (1999) method, which describes anisotropic microstrain broadening. This approach improved the quality of fit, as highlighted in Fig. 3(*c*), but did not significantly change the refined atomic coordinates. Anisotropic microstrain could indicate the presence of defects within the $(Al,Mg)_3La$ crystallites, or the effects of lattice mismatch between $(Al,Mg)_3La$ and the α-Mg matrix. Alternatively, the anisotropic broadening could be due to the plate-like morphology of the small eutectic particles (*i.e.* anisotropic crystallite size broadening). The data do not support a detailed peak profile analysis and further work is required to elucidate this point.

The crystal structure consists of La atoms coordinated with 14 Al(Mg) atoms, 12 of which are arranged in two hexagonal rings with plane normals aligned parallel to the *a*-axis of the unit cell. The two remaining Al atoms lie in the same plane (*bc*) as the La atom. This Al(Mg) atom packing arrangement is consistent with other Al–La intermetallic phases such as $Al_{11}La_3$. The Al–La interatomic distances range from 3.31 to 3.53 Å, which is significantly larger than in the hexagonal Al_3La phase (2.98–3.32 Å, Ni_3Sn-type structure) and more similar to that observed in the $Al_{11}La_3$ phase (3.27–3.78 Å). The incorporation of a low concentration of Mg atoms into the $(Al,Mg)_3La$ phase may account for the slightly larger Al(Mg) to La distances, compared with Al_3La, due to the larger radius of Mg relative to Al. The Al–Al and La–La interatomic distances are in the ranges 2.51–3.10 Å and 4.34–4.52 Å, respectively, which also compares well with the distances observed in Al_3La and $Al_{11}La_3$.

The proposed structure was verified by atomic scale HAADF-STEM imaging, shown in Fig. 5. In Figs. 5(*c*) and 5(*d*), each bright dot represents a column rich in La atoms because the intensity of HAADF-STEM imaging is approximately proportional to the square of the atomic number (Pennycook & Jesson, 1992) (the atomic number is 12 for Mg, 13 for Al and 57 for La). The Al(Mg) atoms are also detected around the much brighter La atoms, but with weaker contrast. Needless to say, it is impossible to distinguish Al atoms from Mg atoms in the HAADF-STEM images. The atom arrangements viewed along these two directions are consistent with those in the proposed structure shown in Figs. 5(*a*) and 5(*b*).

Lastly, samples of this alloy were heat treated at 350°C for 500 h and at 500°C for 100 h to investigate the thermal stability of the $(Al,Mg)_3La$ phase. Conventional XRD data and SEM data collected from these samples also showed two-

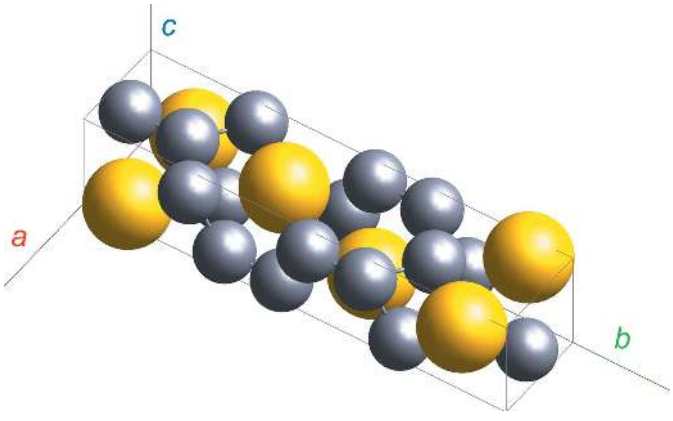

Figure 4
Proposed structure of the $(Al,Mg)_3La$ phase. Al(Mg) and La atoms are represented as silver and yellow balls, respectively.

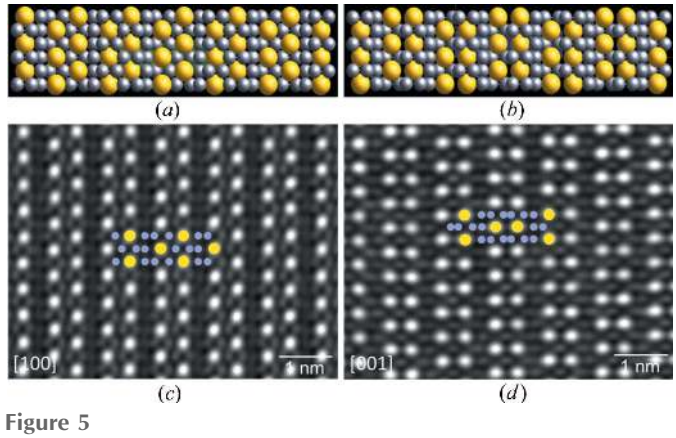

Figure 5
Perspective views of the proposed structure of the $(Al,Mg)_3La$ phase along (*a*) [100] and (*b*) [001] directions compared with atomic scale HAADF-STEM images along (*c*) [100] and (*d*) [001].

phase microstructures consisting of α-Mg and $(Al,Mg)_3La$, indicating that $(Al,Mg)_3La$ is an equilibrium phase in the Mg–Al–La system.

4. Conclusions

A new intermetallic phase has been identified in the Mg–Al–La system, which has the composition of $(Al,Mg)_3La$. The crystal structure has been resolved using high-resolution synchrotron X-ray powder diffraction to be orthorhombic with space group $C222_1$ and lattice parameters a = 4.3365 (1), b = 18.8674 (4) and c = 4.4242 (1) Å. The resolved unit-cell parameters and atom occupancy have been verified by HAADF-STEM imaging and there is an excellent agreement between the two techniques. The Al(Mg) atom packing arrangements of the $(Al,Mg)_3La$ phase are consistent with those of the other Al–La intermetallic phases such as $Al_{11}La_3$.

Acknowledgements

The authors would like to thank Professor Kazuhiro Nogita and Professor Jian-Feng Nie for their support for this project. Part of this research was undertaken on the Powder Diffraction beamline at the Australian Synchrotron, Victoria, Australia (Experiment 12184). The authors wish to thank Mr Carmelo Todaro, Mr Jackson Smith and Dr Aaron Seeber for experimental assistance. Monash Centre for Electron Microscopy (MCEM) is acknowledged for access to experimental facilities.

Funding information

The following funding is acknowledged: Australian Research Council (grant No. LP130100828).

References

Ansara, I., Chart, T., Guillermet, A. F., Hayes, F., Kattner, U., Pettifor, D., Saunders, N. & Zeng, K. (1997). *Calphad*, **21**, 171–218.
Appa Rao, B., Kistaiah, P., Rajasekhar Reddy, N. & Satyanarayana Murthy, K. (1982). *J. Mater. Sci. Lett.* **1**, 432–434.
Bai, J., Sun, Y., Xue, F. & Qiang, J. (2012). *Mater. Sci. Eng. A*, **552**, 472–480.
Bergamaschi, A., Cervellino, A., Dinapoli, R., Gozzo, F., Henrich, B., Johnson, I., Kraft, P., Mozzanica, A., Schmitt, B. & Shi, X. (2010). *J. Synchrotron Rad.* **17**, 653–668.
Bruker (2014). *TOPAS*. Bruker AXS, Karlsruhe, Germany.
Buschow, K. (1965). Philips Research Report, No. 20.
Cacciamani, G. & Ferro, R. (2001). *Calphad*, **25**, 583–597.
Coelho, A. A. (2000). *J. Appl. Cryst.* **33**, 899–908.
Evdokimenko, V. I. & Kripyakevich, P. I. (1963). *Kristallografiya*, **8**, 186–193.
Garde, C., Ray, J. & Chandra, G. (1993). *J. Alloys Compd.* **198**, 165–172.
Gomes de Mesquita, A. H. & Buschow, K. H. J. (1967). *Acta Cryst.* **22**, 497–501.
Guo, C. & Du, Z. (2004). *J. Alloys Compd.* **385**, 109–113.
Havinga, E. (1975). *J. Less Common Met.* **41**, 241–254.
Hosseinifar, M. & Malakhov, D. V. (2010). *J. Alloys Compd.* **505**, 459–466.
ICDD (2017). PDF-4. International Centre for Diffraction Data, Newtown Square, PA, USA.
Jin, L., Kevorkov, D., Medraj, M. & Chartrand, P. (2013). *J. Chem. Thermodyn.* **58**, 166–195.
Kleber, W., Wooster, W. A. & Wooster, A. (1970). *An Introduction to Crystallography*. VEB Verlag Technik.
Klug, H. P. & Alexander, L. E. (1975). *X-ray Diffraction Procedures for Polycrystalline and Amorphous Materials*, 2nd edition. New York: Wiley-Interscience.
Korst, W. L. & Warf, J. C. (1966). *Inorg. Chem.* **5**, 1719–1726.
Liang, P., Su, H.-L., Donnadieu, P., Harmelin, M., Quivy, A., Ochin, P., Effenberg, G., Seifert, H., Lukas, H. & Aldinger, F. (1998). *Z. Metallkd.* **89**, 536–540.
Luo, A. A. (2004). *Int. Mater. Rev.* **49**, 13–30.
Odinaev, K. O., Ganiev, I., Kinzhibalo, V. & Tyvanchuk, A. (1988). *Izv. Vyss. Uchebn. Zaved. Tsvetn. Met.* **2**, 81–85.
Pawley, G. S. (1981). *J. Appl. Cryst.* **14**, 357–361.
Pennycook, S. & Jesson, D. (1992). *Acta Metall. Mater.* **40**, S149–S159.
Pierre, J., Galera, R. & Siaud, E. (1985). *J. Phys. Fr.* **46**, 621–626.
Raghavan, V. (2008). *J. Phase Equilib. Diffus.* **29**, 270–271.
Rietveld, H. M. (1969). *J. Appl. Cryst.* **2**, 65–71.
Rogl, P. (1988). In *Ternary Alloys: a Comprehensive Compendium of Evaluated Constitutional Data and Phase Diagrams*, edited by G. Petzow & G. Effenberg. Weinheim, New York: VCH.
Rossi, A. & Iandelli, A. (1934). *Atti Accad Naz. Lincei Cl. Sci. Fis. Mat. Nat. Rend.* **19**, 415–420.
Rowles, M. R. (2010). *Powder Diffr.* **25**, 297–301.
Rzychoń, T., Kiełbus, A. & Lityńska-Dobrzyńska, L. (2013). *Mater. Charact.* **83**, 21–34.
Samson, S. & Gordon, E. K. (1968). *Acta Cryst.* B**24**, 1004–1013.
Saunders, N. (1990). *Calphad*, **14**, 61–70.
Schobinger-Papamantellos, P. & Fischer, P. (1970). *Naturwissenschaften*, **57**, 128–129.
Stephens, P. W. (1999). *J. Appl. Cryst.* **32**, 281–289.
Sung Bae, J., Kil Choo, W. & Hee Lee, C. (2004). *J. Eur. Ceram. Soc.* **24**, 1291–1294.
Villars, P. & Calvert, L. D. (1991). *Pearson's Handbook of Crystallographic Data for Intermetallic Phases*. Materials Park, OH: ASM International.
Wallwork, K. S., Kennedy, B. J. & Wang, D. (2007). *AIP Conf. Proc.* pp. 879–882.
Wood, D. H. & Cramer, E. M. (1965). *J. Less-Common Met.* **9**, 321–337.
Yin, F., Su, X., Li, Z., Huang, M. & Shi, Y. (2000). *J. Alloys Compd.* **302**, 169–172.
Zarechnyuk, O., Kinzhibalo, V., Tyvanchuk, A. & Rykhal, R. (1981). *Izv. Akad. Nauk. SSSR Met.* pp. 221–223.
Zhou, S. H. & Napolitano, R. E. (2006). *Acta Mater.* **54**, 831–840.
Zhu, S., Easton, M. A., Abbott, T. B., Gibson, M. A. & Nie, J. F. (2016). *Adv. Eng. Mater.* **18**, 932–937.
Zhu, S., Easton, M. A., Abbott, T. B., Nie, J.-F., Dargusch, M. S., Hort, N. & Gibson, M. A. (2015). *Metall. Mater. Trans. A*, **46**, 3543–3554.